Lawrence Berkeley National Laboratory
LBL Publications

Title
Towards the usage of quarry blasts as an active seismic source for subsurface characterization and imaging

Permalink
https://escholarship.org/uc/item/1153f934

Journal
Geophysical Journal International, 235(3)

ISSN
0956-540X

Authors
Li, Peiyao
Nakata, Nori
Kolawole, Folarin
et al.

Publication Date
2023-09-18

DOI
10.1093/gji/ggad391

Copyright Information
This work is made available under the terms of a Creative Commons Attribution License, available at https://creativecommons.org/licenses/by/4.0/

Peer reviewed

eScholarship.org Powered by the California Digital Library
University of California

Geophysical Journal International

Geophys. J. Int. (2023) **235,** 2916–2926
Advance Access publication 2023 October 04
GJI Seismology

https://doi.org/10.1093/gji/ggad391

Towards the usage of quarry blasts as an active seismic source for subsurface characterization and imaging

Peiyao Li,[1] Nori Nakata,[2,3] Folarin Kolawole,[4] Brett M. Carpenter[5] and Hongrui Qiu [3]

[1]*Department of Geophysics, Colorado School of Mines,* 1500 *Illinois Street, Golden, CO* 80401*, USA. E-mail: lipeiyao@mines.edu*
[2]*Department of Earth, Atmospheric and Planetary Sciences, Massachusetts Institute of Technology,* 77 *Massachusetts Avenue,* 54-918*, Cambridge, MA* 02139*, USA*
[3]*Lawrence Berkeley National Laboratory, 1 Cyclotron Road,* 74R316C *Berkeley, CA* 94720*, USA*
[4]*Department of Earth and Environmental Sciences, Lamont-Doherty Earth Observatory of Columbia University,* 61 *Route* 9 *W, Palisades, NY* 10964*, USA*
[5]*School of Geosciences, University of Oklahoma,* 100 *East boyd Street, RM* 710*, Norman, OK* 73019*, USA*

Accepted 2023 September 15. Received 2023 September 10; in original form 2023 April 4

SUMMARY

Active or man-made seismic sources are often used to delineate subsurface geological structures via seismic imaging techniques. Although conventional controlled seismic sources have provided high-resolution subsurface images, the high cost of data acquisition necessitates improved use of cheaper alternative seismic sources for subsurface imaging, such as traffic noise, quarry blasts and earthquakes. Here, we explore the potential use of quarry blasts as an active seismic source for subsurface imaging. The goal of our study is to demonstrate the utility of quarry blasts as seismic sources for investigating subsurface structure with a field experiment in Mill Creek, southern Oklahoma. We deployed a 7455-m-long receiver line of 72 receivers (105 m spacing) extending away from a quarry, with a recording time of 28 d. We analyse similarities between blasts, wave types, origin time and excitation location of quarry blasts, which is important information for using such signal as an active source. Given a relative homogeneous geological condition in the study area, we could not observe clear reflected waves. However, the use of *P*- and *S*-wave velocities led to the delineation of a major basement damage zone in the study area, which further demonstrates the viability of quarry blasts as a useful seismic source for subsurface geological imaging.

Key words: Crustal imaging; Induced seismicity; Quarry blast; Seismic imaging; Wave propagation.

INTRODUCTION

Active seismic sources, such as vibroseis, dynamite explosions and airguns, are categorized as man-made sources. Conventionally, they are utilized for illuminating the Earth's shallow crustal structure (< 10 km) via seismic imaging. However, numerous types of potential seismic sources are not primarily intended for seismic exploration, such as army weapon tests, quarry blasts (Hawman 2004), vehicles (Kuzma *et al.* 2009), railways (Nakata *et al.* 2011) and natural sources like ocean waves and earthquakes (Nakata & Shelly 2018). Although these signals are not intended for seismic imaging of the subsurface, we can leverage these signals for seismic imaging when we captured by seismic receivers, especially when deployed in dense arrays. Exploiting these signals is accomplished by knowing essential information such as the origin time and location, then applying appropriate algorithms and image conditions (i.e. wave-mode extrapolation/separation). It is also essential to quantify the source's energy level, wave type and the wave velocity. For complicated signals (i.e. ocean-related ambient noise), cross-correlation can be used to extract coherent signals.

To identify the aforementioned signals, we often need to stack or apply correlation or beamforming. However, given the rapid technological advancement in the past decades, the capability of geophones to capture a signal at lower frequencies has significantly improved (Brenguier *et al.* 2016). The advantages of such broadband geophones are due to the large flat passband and high dynamic range. Therefore, relatively cheap but dense geophone arrays shall provide an alternative recording option.

Differentiation of quarry blast signals from earthquake signals has been studied (Shashidhar *et al.* 2014; Fereidoni & Atkinson 2017; Li *et al.* 2017). In a quarry blast, explosives are distributed along a wall of rock and detonated in a delayed fashion to control the movement of the rock. In contrast, an earthquake's source signature depends on the shear failure and its theoretical source model space (Brune 1970). Also, methods have been developed to isolate the quarry blasts from catalogues that incorporate the seismic spectra

© The Author(s) 2023. Published by Oxford University Press on behalf of The Royal Astronomical Society. This is an Open Access article distributed under the terms of the Creative Commons Attribution License (https://creativecommons.org/licenses/by/4.0/), which permits unrestricted reuse, distribution, and reproduction in any medium, provided the original work is properly cited.

Downloaded from https://academic.oup.com/gji/article/235/3/2916/7289239 by guest on 06 September 2024

(Yilmaz *et al.* 2013), where the corner frequency of the spectra from a delayed quarry blast is lower than a microseismic event with the same energy release (McLaughlin *et al*. 2004). For a non-delay quarry blast (shots excited at the same time), the spectra show lower energy than a similar magnitude earthquake event (Smith 1993). The seismic source used for mining and quarry exploration is explosive, thus, corresponding to a compressional type of seismic source. This explosive source is used to spall the rock face for exploitation. Despite the considerable amount of seismic energy associated with quarry blasts, their use for subsurface seismic imaging has been limited. Proper utilization of quarry blasts as an active source and careful analysis of the signals generated from the blast may show this source type as economical and efficient in application to the understanding of subsurface geological structure.

In southern Oklahoma, we utilize seismic waves from quarry blasts to examine the associated wave types and extract information vital for active-source imaging, such as the origin time and blast location. Further, we discuss the implications of our results for the observed subsurface structure in the area. The proposed technique in this paper can be applied to quarry blasts in other areas provided that the required information is available.

STUDY AREA AND DATA ACQUISITION

Geology of the study area

The study area is located in the Mill Creek–Tishomingo region of southern Oklahoma (Fig. 1a). It is situated near the core of the Late Palaeozoic Arbuckle Uplift. In this region, the deep Precambrian granitic basement is exposed through hummocky outcrops, surrounded by the overlying folded and faulted Palaeozoic sedimentary rocks (Ham *et al.* 1964; Bickford *et al.* 2015; Kolawole *et al.* 2019). These basement rocks, part of the 1350–1400 Ma Southern Granite–Rhyolite province of the US mid-continent and are composed of granites, rhyolites and their metamorphic derivatives (Bickford *et al.* 2015). Since its emplacement in the Early Proterozoic, the basement has undergone multiple phases of tectonic deformation that include a rifting episode in the Late Proterozoic to Middle Cambrian that resulted in the development of a NW-SE trending magmatic rift system in southern Oklahoma, known as the Southern Oklahoma Aulacogen (Brewer *et al.* 1983; Chase *et al.* 2022). In the Late Palaeozoic, basement-involved transpressional tectonics resulted in the inversion of the rift-bounding faults and basement-cored uplifts in southern Oklahoma. Among those is the Arbuckle Uplift (Brewer *et al.* 1983; Turko & Mitra 2021; Chase *et al.* 2022).

The Arbuckle Uplift comprises several anticlinal domains. One notable feature is the Tishomingo Anticline, at whose centre the Precambrian basement is exposed over an area of ∼300 km^2. Folded Palaeozoic sedimentary units surround the exposed basement region. These units are delineated by dominant NW-SE striking (∼300°/120°) strike-slip and reverse faults (Ham *et al.*1964; Turko & Mitra 2021; Turko & Tapp 2021). Exposed basement regions feature granites, granodiorites and gneisses. These are locally intersected by subvertical and subhorizontal pegmatite and diabase intrusions of Precambrian and Cambrian ages (Lidiak, Denison, & Stern 2014). The predominant NW-SE trend of subvertical dykes was influenced by the pre-existing structural fabric of the Precambrian basement (Lidiak, Denison, & Stern 2014; Kolawole *et al.* 2019). Field observations indicates that the pre-existing basement deformation predominantly features subvertical (dykes) and sub-horizontal (sills) diabase igneous intrusions as depicted in Fig. 1(b), discrete domains of high-intensity fracture intersections, and ∼260-m-wide fault damage zones of dense parallel fracture clusters and hydrothermal mineralization (Kolawole *et al.* 2019, 2020). Although diabase sills in basement exposures in southern Oklahoma are generally <5 m thick (Fig. 1b), deep seismic reflection images in north-central Oklahoma show ∼17-km-thick diabase sills (Kolawole *et al.* 2020).

Seismic data acquisition setup

The objective of our study is to use quarry blasts as the active seismic source to obtain the subsurface structure in the area around the quarry. We designed an EW-oriented straight line along the State Route 7, spanning a total of 7455 m and deployed 72 Fairfield three-component nodes in a temporary dense linear array with 105 m spacing. The first node of the array is located 120 m to the east of the quarry's edge (Fig. 1a). To capture more than one quarry blast and compare the similarity of the sources, we set an acquisition period of 28 d, from 2018 April 15 to May 11. The sampling frequency was set to 500 Hz with a sensitivity to 12 dB, and we used particle velocity as the measurand unit. During the 28 d, we recorded three blasts. The quarry operator provided the blasting times in the local time that were accurate to a minute: 13:22 on April 17, 15:30 on April 26 and 16:00 on May 7. However, the precise detonation times for each blast remain unclear, necessitating source-time estimation from the recorded data. It is worth noting that the exact time and date of the blasts are not essential as the data can be scanned to identify the individual blast events.

The normalized shot gathers, recorded in the vertical component and denoted as UD component for each blast, are displayed in Fig. 2, where *P* and *S* waves are marked by red and green dotted line, respectively. Each trace is normalized according to the absolute maximum among all the traces in each gather (a malfunction in the 12th geophone resulted in the missing trace). As we do not have the precise excitation time and location for each source, we set the onset time at 0 s for each gather to indicate the time where the first receiver in the array initially captured the quarry blast signal. The onset time, with high precision, is based on the assumption that different waves excite simultaneously.

OBSERVED SEISMIC WAVEFIELDS

Frequency spectra and energy level

We compared signals of quarry blasts with the data recorded in non-blast time (i.e. mainly noise) to identify the frequency band of the blast signals and estimate the signal-to-noise ratio. We used the power spectral density (PSD) analysis to evaluate each blast's dominant frequency range and energy level. This analysis allowed us to determine the predominant frequencies for each blast and each component by comparing them with the probabilistic PSD (PPSD) of ambient noise (McNamara & Buland 2004). We then used an appropriate frequency range to enhance the signal-to-noise ratio by applying a bandpass filter. To adequately capture the blast energy, we compute the spectra using the first station closest to the quarry.

For the characteristics of the noise spectra at low frequencies (e.g. <0.1 Hz), we evaluate the PPSD of the continuous recordings using a 3-min-long moving window with 50 per cent overlap. Although three minutes is long compared to the quarry blast, the PPSD shows a significant increase during the blast as discussed below. To obtain a statistically reliable PPSD of the recorded ambient noise rather than

Downloaded from https://academic.oup.com/gji/article/235/3/2916/7289239 by guest on 06 September 2024

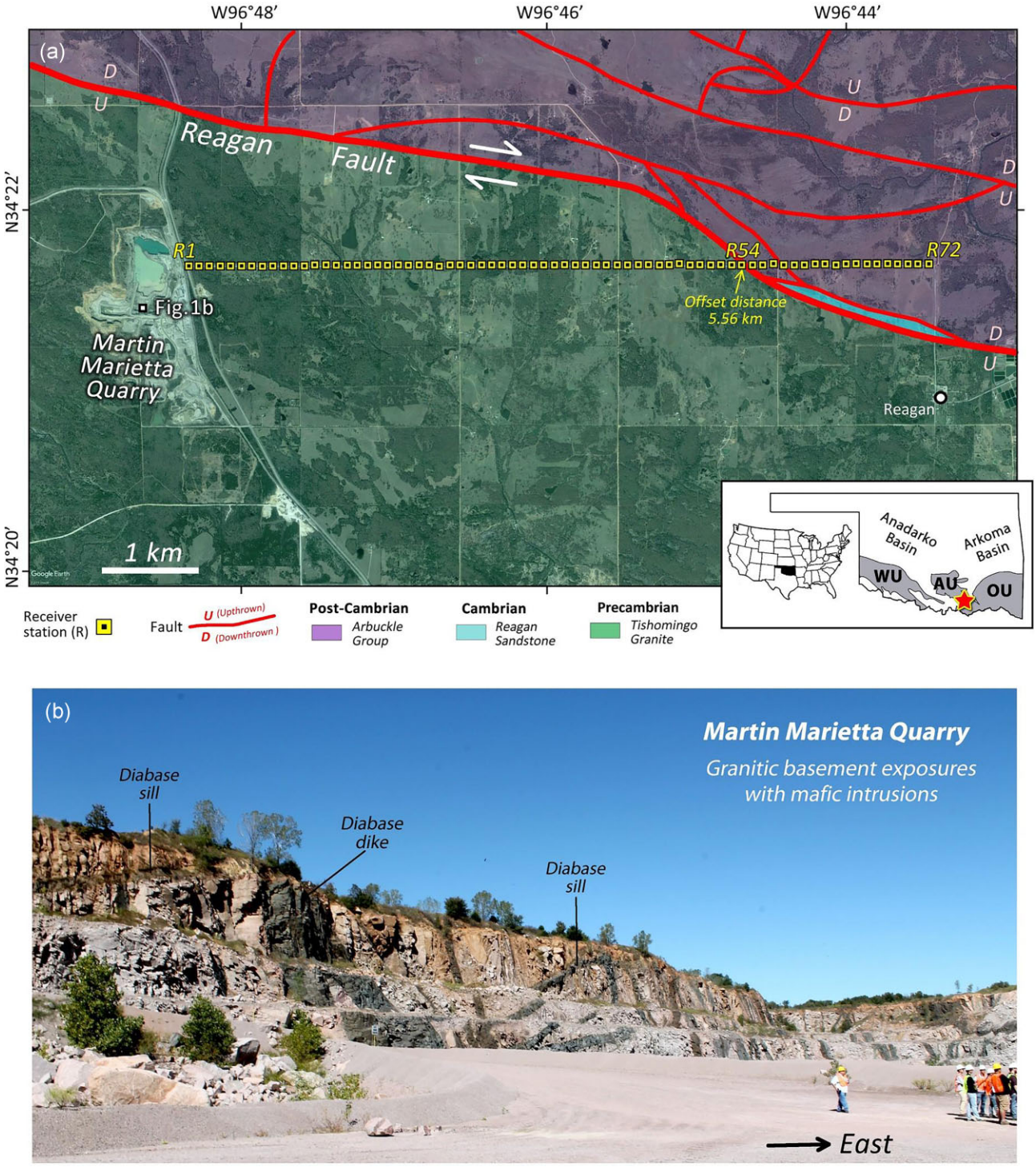

Figure 1. (a) Satellite image (Google Earth) of the study area, overlaid with generalized basement geology (after Ham & McKinley 1954) and the receiver array. Inset: map of US and Oklahoma showing the location of the study area (red star); AU = Arbucke uplift, OU = Ouachita Uplift and WU = Wichita Uplift. Marker 1b point to the location of the quarry in panel (b). (b) Photograph showing surface exposures of the granitic basement at the Martin Marietta Quarry. Light-coloured rocks are granite, and dark-coloured subvertical and dipping bands are diabase dykes and sills. Note that the sills are generally <5 m thick.

the effect of a single noise realization, we calculate the PPSD over an 8-hr-long period around the onset time of each blast. Since no significant seismic events are observed based on visual inspection of all three components, the resulting PPSD is representative of the background noise and blast signal for each shot (Fig. 3). Considering the duration of the blast signal is less than one minute, only 1–2 (out of 319) windows used in the PPSD analysis contain the blast signal. Thus, we take the median of each component's computed PPSD to represent the PSD of the background noise for each component (black curves in Fig. 3). For comparison, we calculate the PSD of the blast signal at the closest receiver by extracting 3-min data that contain the blast wavefields (red dashed curves in Fig. 3). Before

Downloaded from https://academic.oup.com/gji/article/235/3/2916/7289239 by guest on 06 September 2024

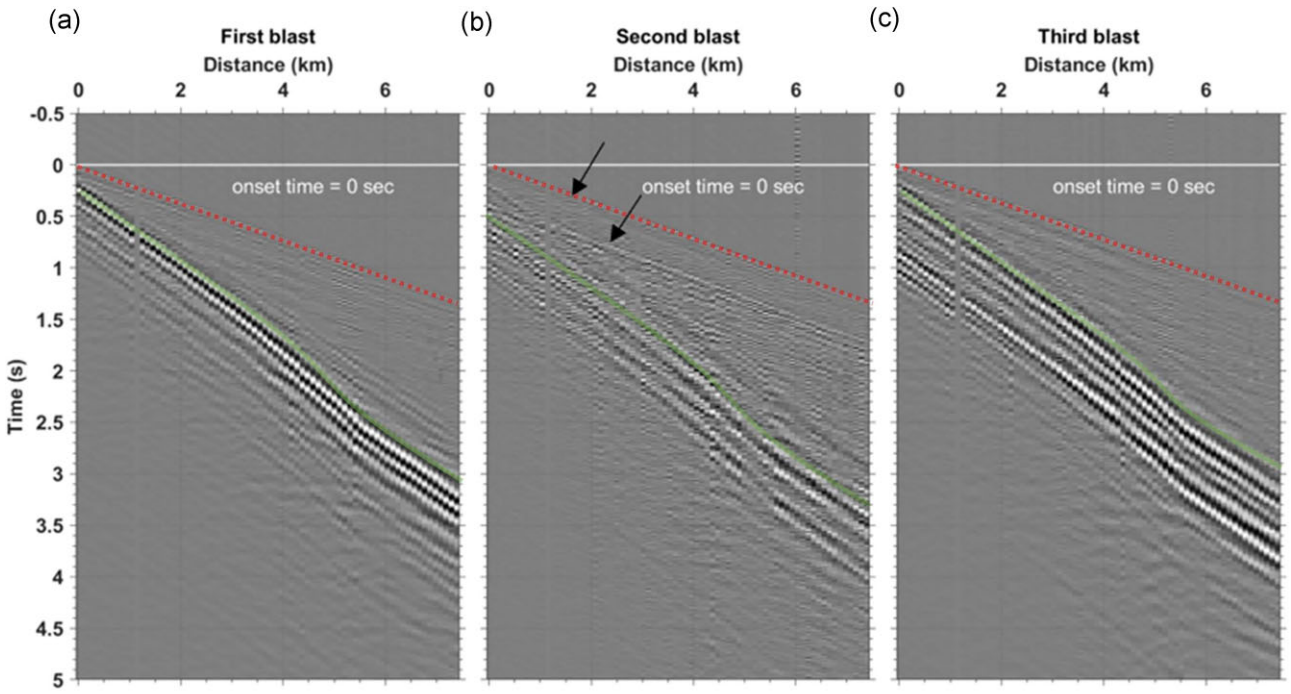

Figure 2. Shot gathers for each blast in the UD component without a bandpass filter. The onset time, estimated below in Table 1, is set to be 0 s in each panel, indicating when we first observe the seismic signal. Red-coloured-dotted line indicates *P* wave and green colour indicates *S* wave. The first receiver is shown as 0 km. Amplitudes of each panel are normalized according to their absolute maximum among all traces in the panel; therefore, we can compare amplitudes between each panel. The black arrows point to two strong arrivals around 0.3 and 0.5 s. The given blast time is at: (a)13:22, 2018 April 17; (b) 15:30 208 April 26 and (c)16:00 2018 May 7, in CDT.

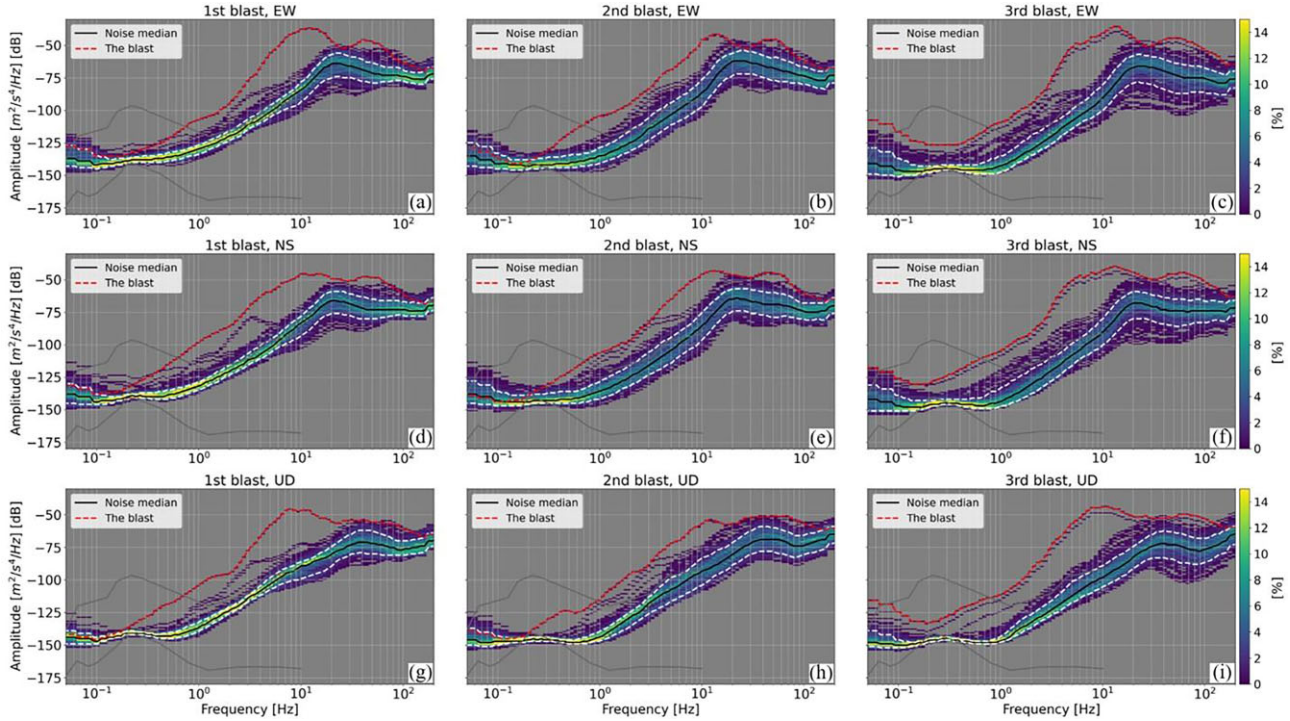

Figure 3. PPSD of 8-hr-long recordings around blasting at the receiver closest to the blast for (a)–(c) east–west, (d)–(f) north–south and (g)–(i) UD components. Areas with a zero probability value are shown in grey. The instrument response is first removed, then a 3-min-long moving window with 50 per cent overlap is used to compute the PPSD shown in each panel. The black curve denotes the median PSD over all analysed windows, whereas the white dashed curves represent the 10th and 90th percentile of the PPSD. The red dashed curve depicts the PSD of the 3-min-long window that contains the blast signal. The background noise model given by Peterson (1993) is illustrated as the grey curves.

Downloaded from https://academic.oup.com/gji/article/235/3/2916/7289239 by guest on 06 September 2024

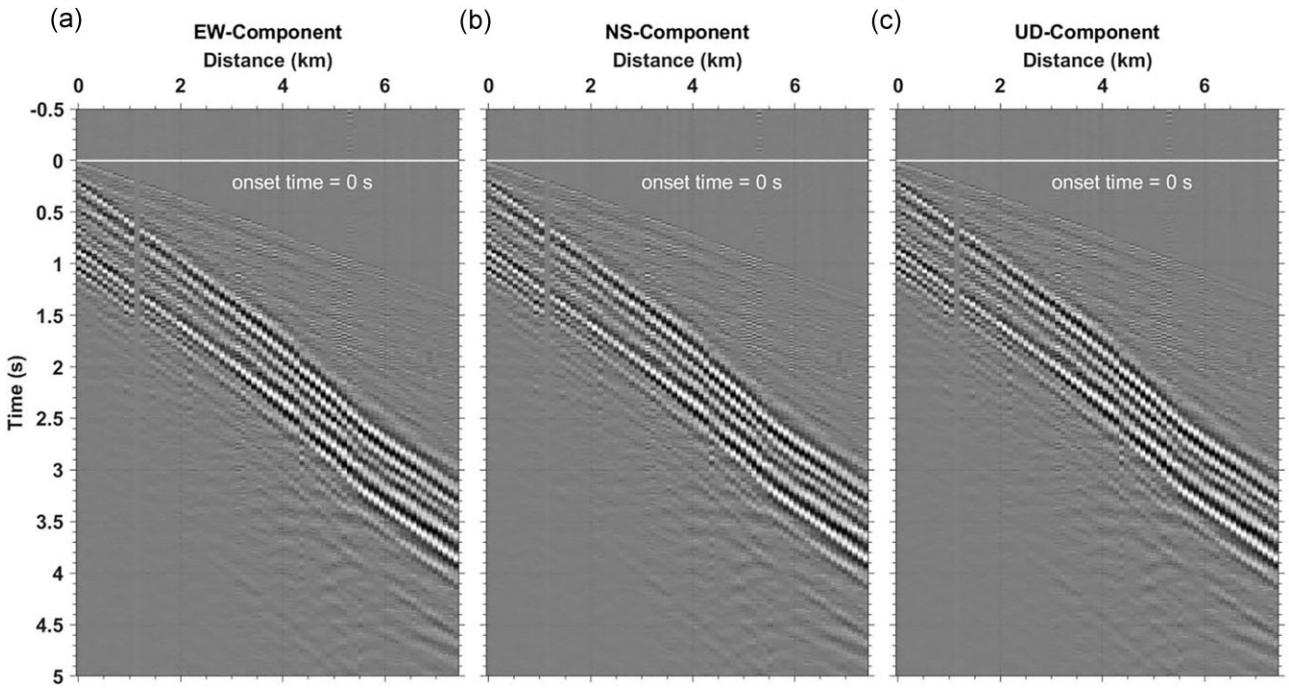

Figure 4. Third blast shot gathers in (a) EW, (b) NS and (c) UD components without any bandpass filters. The onset time in each panel is set to be 0 s, as estimated below. The distance origin is the first receiver. The amplitude of each panel is normalized according to their absolute maximum among all traces in each panel.

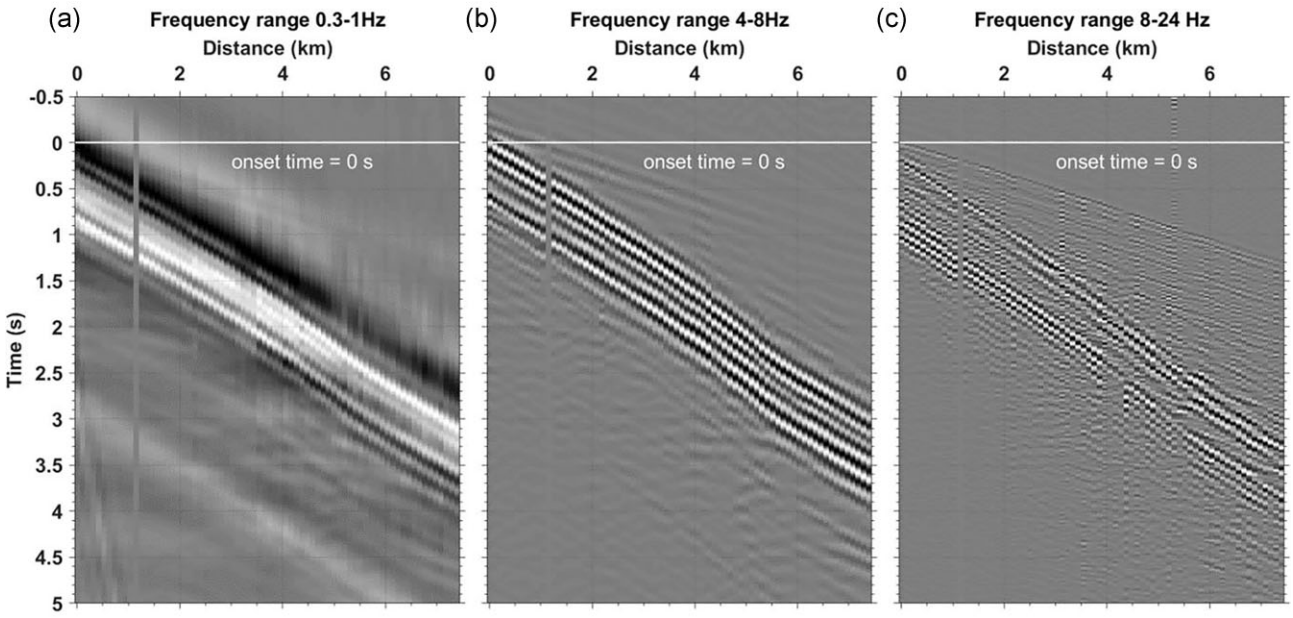

Figure 5. Shot gathers of the third blast in the UD component at different frequency ranges: (a) 0.3–1 Hz, (b) 4–8 Hz and (c) 8–24 Hz. The amplitudes are normalized in each panel. The *S* wave is displayed with larger amplitude at 0.3–1 and 4–8 Hz. Since the wave train arrival change is the same in different frequency ranges, that is, not dispersive, we consider that there is no surface wave.

the PPSD analysis, we removed the instrument response from the continuous recording, producing a power amplitude (Fig. 3) that is directly related to the recorded ground motion.

The predominant blast frequency range is 4–20 Hz, but the signals are observed above background noise levels ranging from 0.2 to 100 Hz (i.e. outside the 10th and 90th percentile range; white dashed curves in Fig. 3). The difference between the black and red dashed curves provides a rough estimation of the signal-to-noise ratio. Importantly, we note that the character of the signal-to-noise ratio does not change much for different components and blast shots. Previous studies also observe that quarry blasts have low frequencies, generally below 20 Hz (Allmann *et al*. 2008), and the lack of high-frequency content is attributable to delayed excitation of the source or strong near-surface attenuation (Allmann *et al.* 2008). The delayed excitation can be viewed as a sequence of single explosions with a time delay between adjacent shots. The purpose of delayed

Downloaded from https://academic.oup.com/gji/article/235/3/2916/7289239 by guest on 06 September 2024

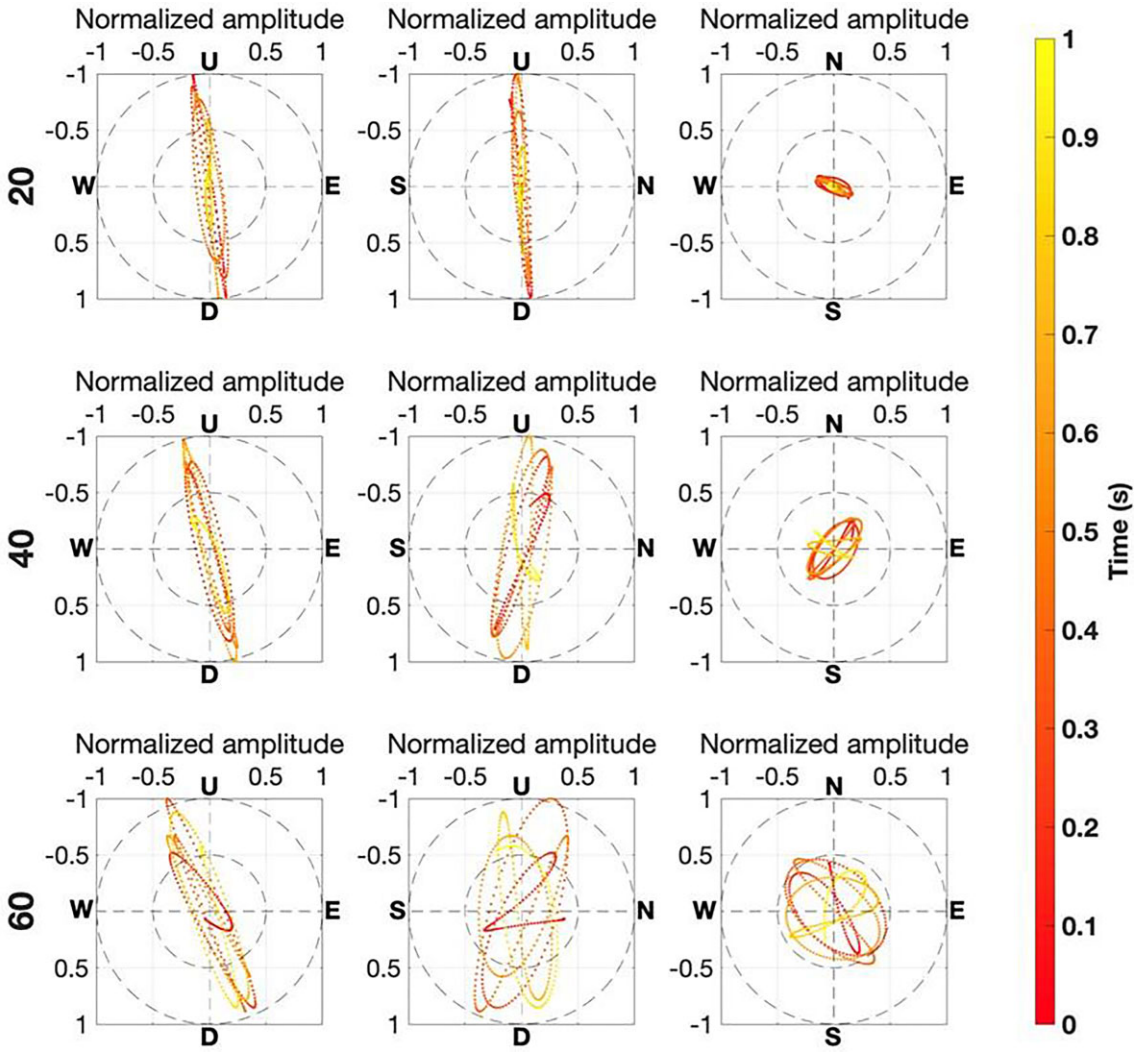

Figure 6. Particle motion for *S* waves within 1 s from the first arrival of the *S* waves at receiver 20th, 40th and 60th from the top to bottom rows. The particle motions of UD-EW, UD-NS and NS-EW components are shown from the left- to right-hand columns. The amplitudes are normalized in each panel. The colour illustrates the time in each window.

detonation is to increase rock fragmentation while decreasing the potential seismic hazards. Due to the periodicity in the delayed excitation, it produces a seismic reinforcement at the frequency of the delay between detonation. Hence, high-frequency content could vanish due to summation.

The PSD analysis provides insight into each blast's energy level. We observe that the power of the third blast is generally the highest among all and is roughly 10^3 times higher than the power of the background noise (Fig. 3). The energy level of the first blast is comparable to the third blast, whereas the second blast has the lowest energy level compared to the other two blasts. The reader should note that even for the second blast, clear signals are observable at the end of the array (7 km away, shown in Fig. 2).

Similarity between different blasts

In addition to the energy level mentioned above, the similarity of the shot gathers can indicate whether changes occur in both the source wavelet and the location of the blasts. Differences in energy levels among the blasts can be normalized. As the variations in the signal from the blast's signals are not our primary focus, identifying the similarities and differences between blasts become crucial for the use of multiple blasts for seismic exploration.

We note that the wave-propagation patterns, such as traveltimes in the gathers, remain consistent across all three blasts. This consistency largely stems from the unchanging structure during the observation period. These patterns are, for example, the change in the slope of wavefields from 4.2 to 5.4 km indicate a velocity decrease at this location.

Identification of wave modes

Since different wave modes sample different components of the elastic moduli and have different sensitivities to the structure, it is necessary to identify *P* and *S* waves for subsurface imaging. Furthermore, we can use these waves to estimate the origin time and the location of blasts. Fig. 4 shows the normalized third shot gathers recorded on all three components.

In addition, for this study, the main recorded energy was *P* waves with a discernible signal above the background noise. In Fig. 5, *P* waves are clearly observed in the 4–8 and 8–24 Hz frequency bands as the first arrivals. This wave arrives at the furthest receiver around

Downloaded from https://academic.oup.com/gji/article/235/3/2916/7289239 by guest on 06 September 2024

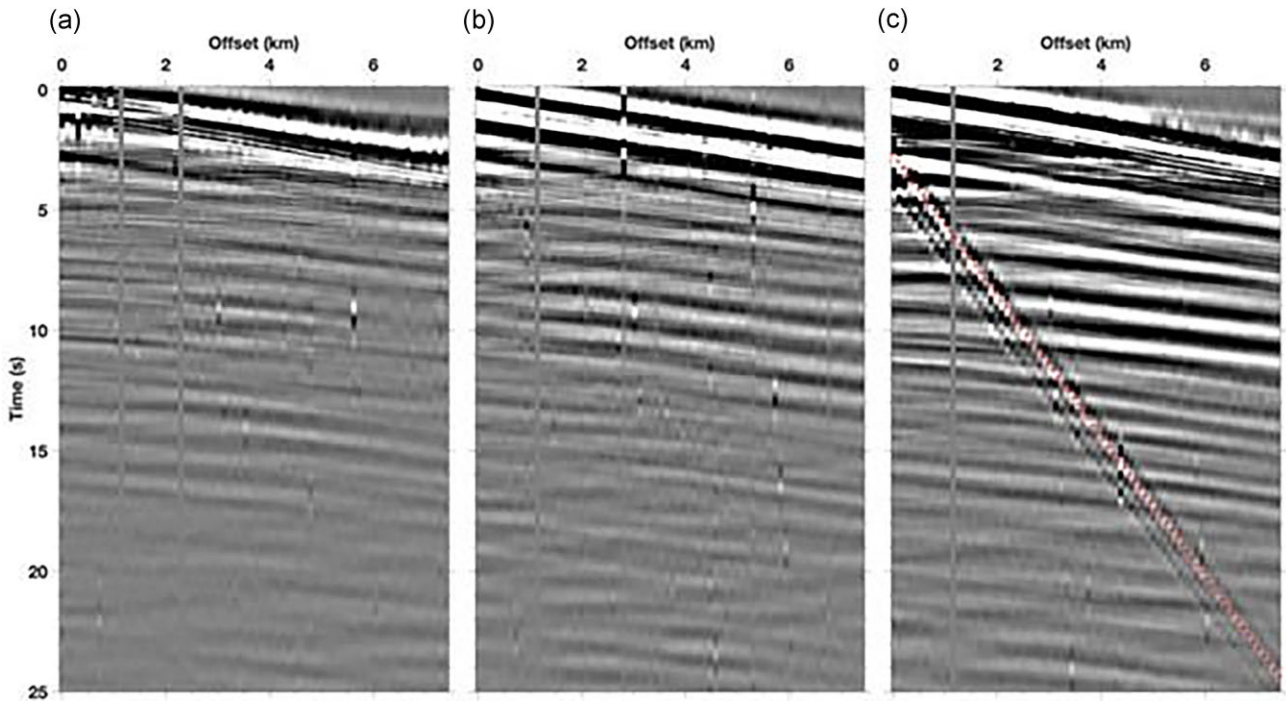

Figure 7. A squared time gain for 0.3–1 Hz frequency band shown in Fig. 5, which aim to bring up weak signals. Different from other figures, the time axis of this figure is between 0–25 s. The linear, longer time duration wave train from 2.5 to 25 s is the air wave from the blast, marked by red semi-transparent, dotted line.

1.4 s, and the apparent phase velocity is approximately 5.5 km s^{-1}, which is within the expected range of velocity for the hard-rock *P* wave. We measure the apparent phase velocities more accurately using the semblance analyses below.

The wave with the highest amplitude shown in Figs 3 and 5, propagating with an apparent phase velocity of approximately 3.0 km s^{-1}, are *S* waves; they are not surface waves for two reasons: first, the surface waves are dispersive, but the observed waves are not, as shown in Fig. 5. Second, the orbit of particle motions in UD-EW and UD-NS panels show almost a linear-elliptical fashion in Fig. 6. For surface waves, it would be elliptical and as source–receiver offset increases, the orbit will eventually become circular which due to the attenuation.

Given the location of the quarry and the geometry of our geophone linearly oriented in the EW direction, we anticipate that the UD and EW components will primarily capture *P*–*SV* waves, with the *SH* waves recorded by the NS component. We can further distinguish between *SV* and *SH* waves using a particle-motion analysis. For the particle-motion analysis, we use a 1-s time window starting from the arrival time of the *S* wave on each receiver and component then plot particle motion for each component pair (Fig. 6). The UD-EW plots show distinct elliptic motions, and the amplitude of the EW component increases with a greater offset increasing (as seen on the 60th receiver in Fig. 6). This pattern suggests that the waves are diving, and thus, the incident angle increases progressively. The NS component does not exhibit a clear correlation with the other two components, and its particle motions illustrate more random behaviour (as observed on the 60th receiver), leading us to concluding that the NS component predominantly contains mostly *SH* waves.

The UD component records air waves (pressure waves travelling along the ground surface) as marked by red dotted–dashed line in Fig. 7(c). Given that the quarry blasts are surface explosive sources, they generate strong pressure waves that can propagate through the air. notably, horizontal components do not capture such waves, as shown in Figs 7(a) and (b). The velocity of these waves is nearly 350 m s^{-1}, aligning with the speed of sound in the air. Due to the airwave's relatively low and predictable speed compared to the subsurface velocities, we intend to use this wave to estimate the origin time and location of the blasts.

All blasts shot gathers show two pronounced events around 0.3–0.5 s in Fig. 2, highlighted by black arrows. Although the *S* wave in the third blast exhibits the most discernible secondary waves, other blasts and wave types also show similar patterns. Their nature remains unclear to us, but since these waves propagate at a nearly consistent speed from the beginning to the end of the array, we hypothesize they originated from the blast sources, not from structural factors.

Origin time and distance

To accurately estimate the true source location and the origin time for each blast, we adopt the semblance analysis (i.e. 1-D beamforming) for *P*, *S* and air waves, since the moveout of these waves are relatively linear in our recorded signals. For semblance analysis, we analyse different possible velocity values and origin times and computing the semblance for each combination. The combination that results in the maximum semblance indicates the most probable velocity and time. Then, we pick the maximum in the semblance gather for each wave. Hence, the maximum represents the square root mean velocity. The semblance-analysis result is shown in Fig. 8, where *P*, *S* and air wave analyses are from left to right, and the components we used are UD, EW and UD respectively. We assume that all the waves are generated by the same source and cover the same distance; hence, we can solve the origin time in the following way:

$$V_{air} * \left(t_{\text{origin}} + t_{\text{air}}\right) = V_s * \left(t_{\text{origin}} + t_s\right) = V_p * \left(t_{\text{origin}} + t_p\right), \quad (1)$$

Downloaded from https://academic.oup.com/gji/article/235/3/2916/7289239 by guest on 06 September 2024

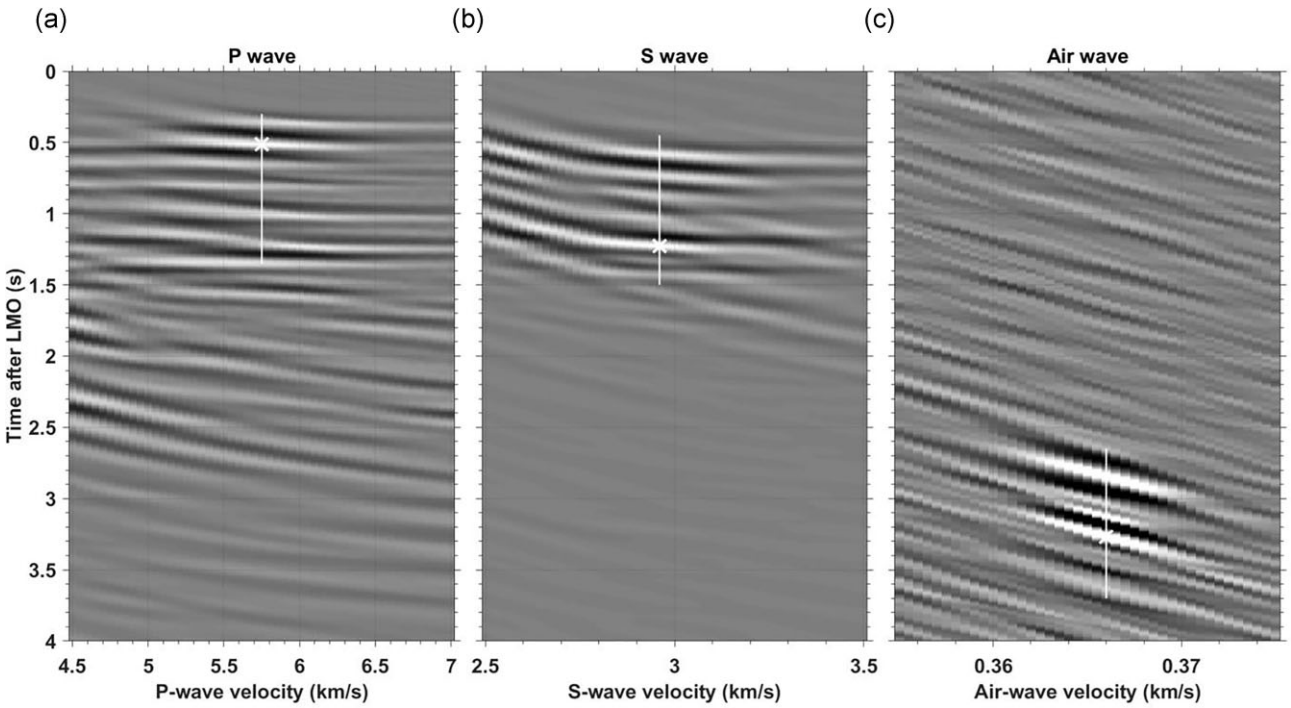

Figure 8. Semblance analysis for the third blast in the for (a) *P*, (b) *S* and (c) air waves. The white line indicates the 1.05-s energy duration for each wave in this blast, and the star indicates the maximum root mean square velocity. The time after the linear moveout correction (LMO) is computed before the onset time.

Table 1. Calculated true excitation time and location for each blast. Note the relative consistency in location of the quarry blast; given that the origin time for the third blast is shortest, we can deduce that the third blast has the highest energy level, proving the validity of semblance analysis.

	Origin time prior to the onset time (s)	Maximum root mean square distance (km)
Blast 1	0.254	1.053
Blast 2	0.3902	0.9656
Blast 3	0.141	0.919

where t_{air}, t_s, t_p and V_{air}, V_s, V_p are obtained from semblance analysis. Thus, we have three equations to solve for one unknown: t_{origin}. Thus, we obtain three t_{origin} values after the calculation, and then we take the mean of all three t_{origin}. Finally, we substitute the estimated t_{origin} into eq. (1) and estimate the distance between the source and the first receiver. The results are shown in Table 1. The accuracy of the estimated of the origin time due to the accuracy of the onset time picking could affect both velocity estimation and reflection imaging especially at the near offset and shallow structure. We estimate both onset time and location of sources. Because the estimated location is reasonable according to the map, the onset time should have reasonable accuracy as well.

DISCUSSION

Velocity variation between 4 and 6 km distance

Inspection of shot gathers indicates a prominent velocity decrease between offset distances of 4.2–6.0 km (Figs 2, 3 and 5). To confirm if the local geology causes this, after we manually picked the traveltimes of the waves, we use second-order central finite-difference scheme with fourth-order error estimation (Fornberg 1988) to calculate the *S*-wave velocity at each geophone location for all blasts and all components. The equation is:

$$\frac{1}{V(x)} = \frac{-F(x+2h)+8F(x+h)-8F(x-h)+F(x-2h)}{12h}, \tag{2}$$

where $F(x)$ is the *S*-wave's traveltime at location x, $F(x+2h)$ is the *S*-wave's traveltime at station $x+2h$, which is $2h$ away to the east of the station located at x and $V(x)$ is the *S*-wave velocity at location x. *S*-wave's traveltime at each receiver is manually picked from the shot gather. *S*-wave slowness at location x, that is, $1/V(x)$, is calculated based on eq. (2). We use the nearest receiver distance as h. By adopting this method, we can minimize the error of picking.

As Fig. 9 shows, for all blasts, the *S*-wave velocity recorded in the NS component is faster than the *S* wave recorded in EW and UD components. Additionally, we find that for all components of all three blasts, the velocity drops significantly between 4.2 and 6.0 km offset distances and reaches a minimum of 5.4–5.6 km. Further east starting from the 6.0 km offset, the values increase up to the background values. Based on the calculated co-located velocity drops across all blasts, we infer an association of this observation with subsurface geology. The geological map of the area (Fig. 1b) shows that a previously mapped major basement-rooted fault zone, Reagan Fault (Ham & McKinley 1954), intersects with our receiver line at an offset distance of $\sim$ 5.6 km (54th receiver). This fault is one of the many $>$ 50-km-long NW-trending strike-slip faults that accommodated Late Palaeozoic left-lateral transpressional tectonic deformation in the region (Turko & Tapp 2021; Chase *et al.* 2022). Detailed 3-D seismic reflection illumination of the fault systems using seismic attributes reveals along-fault deformation zones as

Downloaded from https://academic.oup.com/gji/article/235/3/2916/7289239 by guest on 06 September 2024

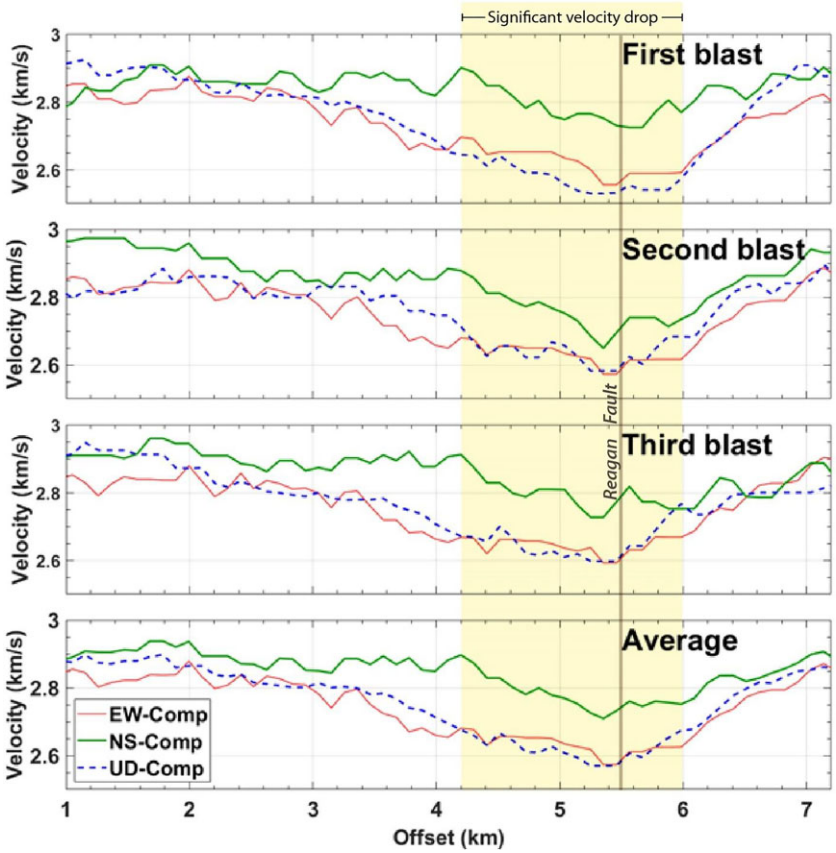

Figure 9. Calculating phase velocity at each receiver for all blasts and all components using first derivative finite-difference calculation with fourth-order estimation. The top three panels show the results for each component at each blast; the bottommost panel represents the mean of all blasts for each component. We observe a gradual, but significant velocity decrease between the 4.2 and 6.0 km offset markers in all the blasts.

wide as ∼ 2.0 km (Turko & Tapp 2021). The collocation of the Reagan Fault with the velocity minima suggests an influence of the fault zone deformation on the subsurface velocity structure at the location of the fault. Studies have shown that the deformation zones of basement-rooted faults can extend up to 1.5 km in width, within which up to a 50 per cent decrease in seismic velocities can be observed (e.g. Cochran *et al*. 2009). This significant velocity decrease is due to the reduction in the shear moduli of the rock associated with intense fracturing, brecciation and increased permeability of the fault zone during the phases of movement along the fault. Therefore, we interpret that the ∼1.8-km-wide zone of velocity drop along our seismic line is most likely associated with the deformation zone of the Reagan Fault, which may or may not include some previously unmapped subsidiary fault segments.

Attenuation

Understanding the attenuation as a function of distance can help us better design the receiver line's geometry to utilize the quarry blast signal properly. As shown in Fig. 10, the black line indicates the normalized power spectrum for the first receiver based on its maximum energy level, and the red line is the normalized power spectrum based on the first receiver's maximum value for the 10th, 40th and 70th receiver's power spectrum for each component from the third blast. The distances from the source location to the selected receiver locations are 1924, 5074 and 8224 m after calculating the origin location of the source. Hence, we can observe that the energy level is decreasing relative to the level at the first receiver, which is 980 m away from the source. To better understand the attenuation in terms of spherical spreading, this study can be suitable for others to design their own acquisition geometry. We apply $1/R$ which is distance between source to receiver for far-field consideration. The calculated power spectra from the first receiver match up well to 10 Hz with a red line. The deviation after 10 Hz can be interpreted as the effect of structural attenuation.

Lack of reflection

Based on the inspection of shot gathers we obtained, we could not find any reflected waves in the gathers. We interpret the lack of reflection as a sign of insufficient impedance contrast between the subsurface formations. The geology of the area where we set the geophone array corresponding to a relatively homogenous crystalline granite, with the dyke and sill intrusions mainly composed of diabase. According to lab measurements, the granite compressional velocity ranges from 5.5 to 6.0 km s^{-1} and diabase from 5.8 to 6.3 km s^{-1} (Kibikas *et al*. 2020). In addition to compressional velocity, the bulk density of granite ranges from 2.60 to 2.62 g cm^{-3} and diabase from 2.62 to 3.00 g cm^{-3}. Therefore, both the velocity and density contrast are very small, and the diabase intrusion structures are relatively thin. Thus, the reflected waves would be difficult to generate. To have a reflected wave, the velocities for the two layers should have a sharp impedance contrast. Due to the differences in *P*-wave velocity and density between the different rocks

Downloaded from https://academic.oup.com/gji/article/235/3/2916/7289239 by guest on 06 September 2024

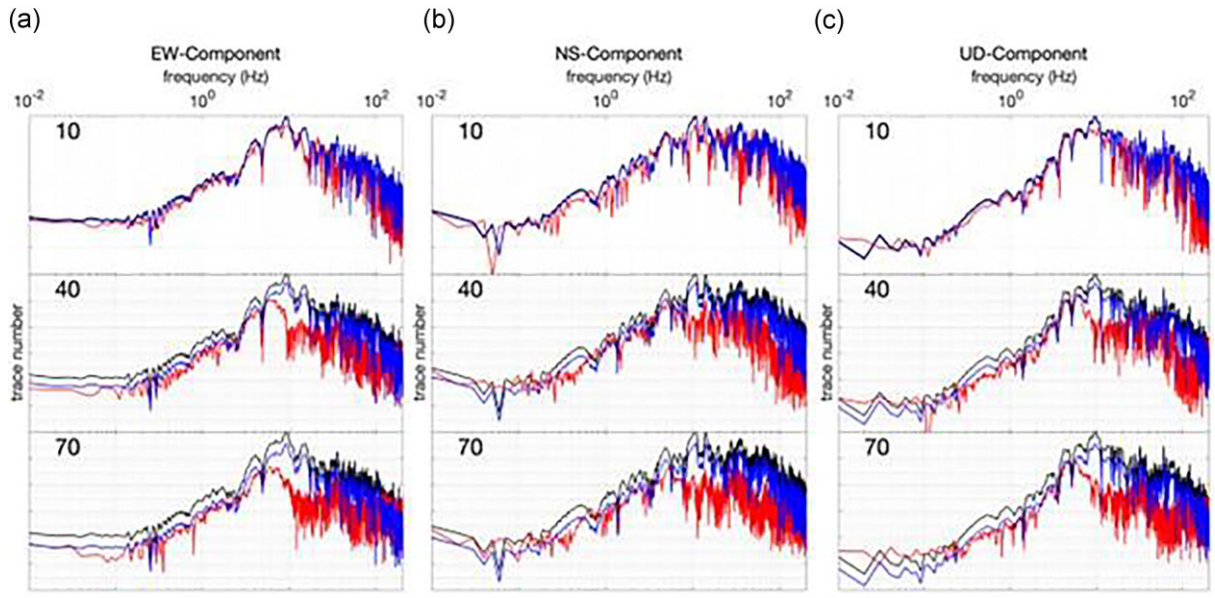

Figure 10. Power spectra for 1st, 10th, 40th and 70th receivers from EW, NS and UD components for the third blast are shown in (a)–(c). In each panel, the black line is the power spectrum from the first recevier, and the red line is the power spectrum corresponding to the receiver number annotated on each figure. We apply $1/R$ for far-field (blue curve) consideration to qualitatively analyse the spherical spreading according to the distance from a calculated source location to the receiver. The calculated power spectra from 1st receiver matches up well to 10 Hz with a red line. The deviation after 10 Hz can be the effect of structural attenuation.

being relatively small, resulting in a small impedance contrast, no reflected waves were produced. Additionally, as the thickness of the sills exposed at the surface is <5 m, and the dykes are generally < 10 m-thick, the resolution of our experiment does not permit us to image such structures.

CONCLUSIONS

Anthropogenic activities can be used as active seismic sources to understand and image the subsurface with calculated origin time and distance. This paper demonstrates the applicability of explosive quarry blasts for subsurface structural imaging. We first design an east–west oriented linear array to record blasts. The wavelength used is mostly longer than the receiver spacing. At 10 Hz (highest blast energy), the wavelength is roughly 260 m. Hence, the aliasing effect is not very severe. Therefore, it was easier for us to pick the traveltimes. When we increase the receiver spacing, aliasing can suffer it. When we use reflected waves, this effect becomes less severe. Additionally, the resolution of the detected faults would be lower too. The study shows that even in the absence of reflected seismic waves, near-surface structural deformation can be characterized using direct waves incorporated with the finite difference method. The occurrence of the air waves provides a more robust constraint other than only using *P* and *S* waves to estimate the source origin time and location, which is necessary information to treat an anthropogenic source as an active source for subsurface imaging. Furthermore, we highlight that the useable frequency range for quarry blasts are in the lower frequency-range confined to a narrower band (4–20 Hz) than the conventional active source (5–40 Hz); thus, requiring a more careful selection of frequency filters.

We incorporated a finite-difference estimation, calculated the *S*-wave velocity at each receiver position, and found that between 4–6 km in our receiver array, there is a gradual velocity decrease, which we interpret as structural damage related to a known, mapped fault zone at the ∼6 km mark. These results demonstrate the viability of quarry blasts as a useful seismic source for subsurface geological imaging.

ACKNOWLEDGMENTS

We thank Raymond Ng for deployment assistance and Martin-Marietta Aggregates for providing the general blast timing information. NN is supported by the U.S. Department of Energy under award number DE-AC02–05CH11231 for this study.

CONFLICT OF INTEREST

The authors declare no conflict of interest.

DATA AVAILABILITY

Data were acquired using Fairfield Zland 3C nodes. The study area is along State Route 7. The data underlying this article will be shared on reasonable request to the corresponding author.

REFERENCES

Allmann, B.P., Shearer, P.M. & Hauksson, E. 2008. Spectral discrimination between quarry blasts and earthquakes in southern California. *Bull. seism. Soc. Am.,* **98**(4), 2073–2079.

Bickford, M.E., Schmus, W.R., Karlstrom, K.E., Mueller, P. & Kamenov, G.D. 2015. Mesoproterozoic-trans-laurentian magmatism: a synthesis of continent-wide age distributions, new SIMS U–Pb ages, zircon saturation temperatures, and Hf and Nd isotopic compositions. *Precambrian Res.,* **265,** 286–312.

Brenguier, F. *et al.* 2016. Toward 4D noise-based seismic probing of volcanoes: perspectives from a large-*N* experiment on Piton de la Fournaise Volcano. *Seismol. Re.s Lett.,* **87**(1), 15–25.

Brewer, J.A., Good, R., Oliver, J.E., Brown, L.D. & Kaufman, S. 1983. COCORP profiling across the Southern Oklahoma aulacogen: overthrusting

Downloaded from https://academic.oup.com/gji/article/235/3/2916/7289239 by guest on 06 September 2024

of the Wichita Mountains and compression within the Anadarko Basin. *Geology,* **11**(2), 109–114.

Brune, J.N. 1970. Tectonic stress and the spectra of seismic shear waves from earthquakes, *J. geophys. Res.,* **75**(26), 4997–5009.

Chase, B.F., Kolawole, F., Atekwana, E.A., Carpenter, B.M., Turko, M., Abdelsalam, M.G. & Finn, C. 2022. *The 180-km-long Meers-Willow Fault System in the Southern Oklahoma Aulacogen: a Potential US Mid-continent Seismic Hazard*. GSA Bulletin.

Cochran, D.L., Bosshardt, D.D., Grize, L., Higginbottom, F.L., Jones, A.A., Jung, R.E., Wieland, M. & Dard, M. 2009. Bone response to loaded implants with non-matching implant-abutment diameters in the canine mandible, *J. Periodontol.,* **80**(4), 609–617.

Fereidoni, A. & Atkinson, G.M. 2017. Discriminating earthquakes from quarry blasts based on shakemap ground-motion parameters, *Bull. seism. Soc. Am.,* **107**(4), 1931–1939.

Fornberg, B. 1988. Generation of finite difference formulas on arbitrarily spaced grids, *Math. Comput.,* **51**(184), 699–706.

Ham, W.E., Denison, R.E. & Merritt, C.A. 1964. Basement rocks and structural evolution of Southern Oklahoma: ABSTRACT, *AAPG Bull.,* **48**(4), 529. doi: 10.1306/BC743C77-16BE-11D7-8645000102C1865D.

Ham, W.E. & McKinley, M.E. 1954. Geologic map and sections of the Arbuckle Mountains, *Oklahoma: Oklahoma Geological Survey Map A−2, scale* **1:72,**000.

Hawman, R.B. 2004. Using delay-fired quarry blasts to image the crust: a comparison of methods for deconvolving mixed-delay source wavelets, *Bull. seism. Soc. Am.,* **94**(4), 1476–1491.

Kibikas, W.M., Carpenter, B.M. & Ghassemi, A. 2020. Mechanical strength and physical properties of Oklahoma's igneous basement, *Tectonophysics,* **777**(20 February 2020), 228336. https://doi.org/10.1016/j.tecto.2020.228336.

Kolawole, F. *et al.* 2019. The susceptibility of Oklahoma's basement to seismic reactivation. *Nat. Geosci.,* **12,** 839–844

Kolawole, F., Turko, M.S. & Carpenter, B.M. 2020. Basement-controlled deformation of sedimentary sequences, Anadarko Shelf, Oklahoma, *Basin Res.* **32**(6), 1365–1387.

Kuzma, H.A., Fernández-Martínez, J.L., Zhao, Y., Dunson, C., Zhai., M.Y., Mangriotis, M.D. & Rector, J.W. 2009. Vehicle traffic as a source for near-surface passive seismic imaging, in *Symposium on the Application of Geophysics to Engineering and Environmental Problems Proceedings,* pp. 609–615. https://doi.org/10.4133/1.3176748.

Li, B., Li, N., Wang, E., Li, X., Zhang, Z., Zhang, X. & Niu, Y. 2017. Discriminant model of coal mining microseismic and blasting signals based on waveform characteristics. *Shock Vib,* 13. https://doi.org/10.1155/2017/6059239.

Lidiak, E.G., Denison, R.E. & Stern, R.J. 2014. Cambrian (?) Mill Creek diabase dike swarm, eastern Arbuckles : a glimpse of Cambrian rifting in the southern Oklahoma aulacogen, *Oklahoma Geol. Surv. Guidebook,* **38,** 105–122.

McLaughlin, K.L., Bonner, J.L. & Barker, T. 2004. Seismic source mechanisms for quarry blasts: modelling observed Rayleigh and Love wave radiation patterns from a Texas quarry, *Geophys. J. Int.,* **156**(1), 79–93.

McNamara, D.E. & Buland, R.P. 2004. Ambient noise levels in the continental United States. *Bull. seism. Soc. Am.,* **94**(4), 1517–1527.

Nakata, N. & Shelly, D.R. 2018. Imaging a crustal low-velocity layer using reflected seismic waves from the 2014 earthquake swarm at Long Valley Caldera, California: the magmatic system roof?, *Geophys. Res. Lett.,* **45**(8), 3481–3488.

Nakata, N., Snieder, R., Tsuji, T., Larner, K. & Matsuoka, T. 2011. Shear wave imaging from traffic noise using seismic interferometry by cross-coherence, *Geophysics,* **76**(6), SA97–SA106.

Peterson, J.R. 1993. *Observations and modeling of seismic background noise (Open-File Report 93–322),* doi:10.3133/ofr93322.

Shashidhar, D., Mallika, K., Rao, N.P., Satyanarayana, H.V.S. & Gupta, H.K. 2014. Detection of quarry blasts in the Koyna-Warna region, western India. *Open J. Earthq. Res.,* **03,** 162–169.

Smith, B.Y.A.T. 1993. Mining blasts, *Society,* **83**(1), 160–179.

Turko, M. & Mitra, S. 2021. Macroscopic structural styles in the southeastern Anadarko Basin, southern Oklahoma. *Mar. Petrol. Geol.,* **125,** 104863.

Turko, M. & Tapp, B. 2021. Structural analysis of the Washita Valley Fault in the southeast Anadarko Basin. *Interpretation,* **9**(1), T183–T200.

Yilmaz, Ş., Bayrak, Y. & Çinar, H. 2013. Discrimination of earthquakes and quarry blasts in the eastern Black Sea region of Turkey, *J. Seismol.,* **17**(2), 721–734.

Downloaded from https://academic.oup.com/gji/article/235/3/2916/7289239 by guest on 06 September 2024

© The Author(s) 2023. Published by Oxford University Press on behalf of The Royal Astronomical Society. This is an Open Access article distributed under the terms of the Creative Commons Attribution License (https://creativecommons.org/licenses/by/4.0/), which permits unrestricted reuse, distribution, and reproduction in any medium, provided the original work is properly cited.